Key Role of d(0) and d(10) Cations for the Design of Semiconducting Colusites: Large Thermoelectric ZT in Cu26Ti2Sb6S32 Compounds

Takashi Hagiwara, Koichiro Suekuni, Pierric Lemoine, Andrew R. Supka, Raju Chetty, Emmanuel Guilmeau, Bernard Raveau, Marco Fornari, Michihiro Ohta, Rabih Al Rahal Al Orabi, et al.

Key Role of d^0 and d^{10} Cations for the Design of Semiconducting Colusites: Large Thermoelectric *ZT* in $Cu_{26}Ti_2Sb_6S_{32}$ compounds

Takashi Hagiwara,[a] Koichiro Suekuni,*[a,b] Pierric Lemoine,[c] Andrew R. Supka,[d] Raju Chetty,[e] Emmanuel Guilmeau,*[f] Bernard Raveau,[f] Marco Fornari,[d] Michihiro Ohta,[e] Rabih Al Rahal Al Orabi,[d] Hikaru Saito,[g] Katsuaki Hashikuni,[a] and Michitaka Ohtaki[a,b]

[a] Department of Applied Science for Electronics and Materials, Interdisciplinary Graduate School of Engineering Sciences, Kyushu University, Kasuga, Fukuoka 816–8580, Japan

*suekuni.koichiro.063@m.kyushu-u.ac.jp

[b] Transdisciplinary Research and Education Center for Green Technologies, Kyushu University, Kasuga, Fukuoka 816-8580, Japan

[c] Université de Rennes 1, CNRS, ISCR-UMR 6226, F-35000 Rennes, France

[d] Department of Physics and Science of Advanced Materials Program, Central Michigan University, Mt. Pleasant, Michigan 48859, USA

[e] Global Zero Emission Research Center, National Institute of Advanced Industrial Science and Technology (AIST), Tsukuba, Ibaraki 305-8569, Japan

[f] CRISMAT, CNRS, Normandie Université, ENSICAEN, UNICAEN, 14000 Caen, France

*emmanuel.guilmeau@ensicaen.fr

[g] Institute for Materials Chemistry and Engineering, Kyushu University, Kasuga, Fukuoka 816-8580, Japan

Thermoelectric material, sulfide, colusite, electronic and thermal transport properties, electronic and phonon structures

ABSTRACT: Cu–S-based materials with sphalerite-derivative structures are of interest for their complex cationic distribution, rich crystal structure chemistry, and their potential in energy conversion, and optoelectronic applications. In this study, a new member of colusite, $Cu_{26}Ti_2Sb_6S_{32}$, was designed by exploiting the key role of d^0 (*T*) and d^{10} (*M*) cations in the sphalerite-derivative structure of $Cu_{26}T_2M_6S_{32}$ colusites. We succeeded to incorporate d^0 Ti^{4+} and d^{10} Sb^{5+}, into *T* and *M* sites respectively, with a tetrahedral coordination rarely found for these two cations in solid-state chemistry. The synthesis produced the first semiconducting compound with the colusite structure. In addition, $Cu_{26}Ti_2Sb_6S_{32}$ exhibits a low lattice thermal conductivity. Partial substitution of Ge for Sb increased the hole carrier concentration, leading to enhanced thermoelectric power factor and dimensionless figure of merit (*ZT* of 0.9 at 673 K). The electronic and phonon structures, responsible for the high thermoelectric performance, were elucidated by first principles calculations.

Introduction

Copper-based sulfides and selenides with sphalerite-derivative structures represent a broad class of materials, whose promising electronic and optoelectronic properties originate from the semiconducting electronic structure and delocalization of hole carriers over a tetrahedral Cu–S/Se framework. Such materials provide a variety of applications such as photovoltaic[1–4] and thermoelectric devices,[5–7] both of which can generate electricity from renewable energy sources (light energy and thermal energy) and are therefore expected to play a critical role toward a sustainable energy economy.

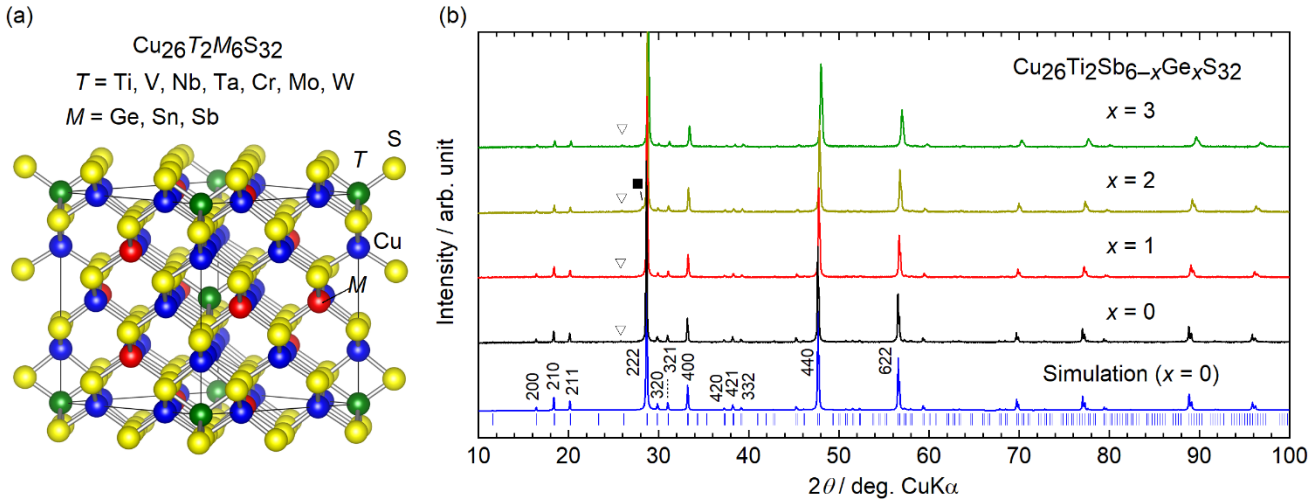

Figure 1. (a) Crystal structure representation of $Cu_{26}T_2M_6S_{32}$ colusites and (b) powder X-ray diffraction patterns of the sintered samples in the $Cu_{26}Ti_2Sb_{6-x}Ge_xS_{32}$ series. The simulated pattern for x = 0 is shown at the bottom. The small peaks denoted by triangles originate from Cu K_β radiation. The square symbol indicates a peak from $Cu_{2-\delta}S$ secondary phase.

Cu–S-based thermoelectric materials have been attracting interest because of the natural-abundant, low-cost, and less toxic characters of their constituent elements, as well as the high thermal-to-electrical energy conversion performance. The best example is represented by the large family of synthetic colusites with the generic formula $Cu_{26}T_2M_6S_{32}$ (T = V, Nb, Ta, Cr, Mo, W and M = Ge, Sn).[8–11] The (synthetic) colusite structure derives from the simple cubic sphalerite structure but exhibits a more complex distribution of the cations (Figure 1a) and a fascinating interplay between the corner sharing Cu–S tetrahedral network and the T sites.[11,12] Indeed, it has been shown that $[TS_4]Cu_6$ complexes within the colusite unit cell form four iono-covalent T–S bonds and six metal like T–Cu interactions with the Cu–S framework with major consequences on the electrical resistivity (ρ) and Seebeck coefficient (S).[11,12] This contributes to the exceptionally high power factor $S^2\rho^{-1}$ up to 1.9 mW K^{-2} m^{-1} at 700 K in $Cu_{26}Cr_2Ge_6S_{32}$.[11,12] Due to the complexity of the structure (large primitive unit cell with 66 atoms), the presence of low frequency Cu optical vibrations, and relatively large anharmonicity (large Grüneisen parameter, γ) of the acoustic vibrations, favor low lattice thermal conductivity (κ_{lat}) of less than 1 W K^{-1} m^{-1} at 700 K.[11,13] The combination of high $S^2\rho^{-1}$ and low κ_{lat} makes this class of materials attractive for thermoelectric energy conversion applications. Indeed, the dimensionless figure of merit $ZT = S^2\rho^{-1}\kappa^{-1}T = S^2\rho^{-1}(\kappa_{lat} + \kappa_{ele})^{-1}T$ reaches values close to the unity at around 700 K in $Cu_{26}V_2Sn_6S_{32}$,[13] $Cu_{26}Nb_2Ge_6S_{32}$,[14] $Cu_{26}Ta_2Sn_{5.5}S_{32}$,[14] and $Cu_{26}Cr_2Ge_6S_{32}$[11] (κ and κ_{ele} are the total and electronic thermal conductivity, respectively).

From an electronic structure perspective, the synthetic colusites discussed in the literature so far are metals (p-type degenerate semiconductors) whose cationic ordering is dictated by the specific chemistry rather than the atomic size. One, indeed, observes that the T site is only occupied by a d^0 cation (V^{5+}, Nb^{5+}, Ta^{5+}, Cr^{6+}, Mo^{6+}, W^{6+}), whereas the M site is occupied by a cation with a d^{10} configuration (Ge^{4+}, Sn^{4+}) exclusively.[8–11] The ability to introduce 4+ and 5+ cations in T and M sites, respectively, can greatly enhance the potential for chemical tuning. Unfortunately, including simultaneously Ti^{4+} as d^0 cation and Sb^{5+} as d^{10} cation in the colusite structure is challenging because these cations do not tend to accommodate in the tetrahedral coordination of sulfur which, to the best of our knowledge, was only observed in Cu_4TiS_4[15] and Cu_3SbS_4[16]. From the formal charge point of view, the additional electrons in $Cu^{+}_{26}Ti^{4+}_{2}Sb^{5+}_{6}S^{2-}_{32}$ compared with $Cu^{+}_{22}Cu^{2+}_{4}T^{5+}_{2}M^{4+}_{6}S^{2-}_{32}$ (T = V, Nb, Ta) and $Cu^{+}_{24}Cu^{2+}_{2}T^{6+}_{2}M^{4+}_{6}S^{2-}_{32}$ (T = Cr, Mo, W), are expected to compensate the delocalized hole carriers leading to the first (pure) semiconducting colusite, which may greatly enhance the applicative impact of this class of environmentally friendly materials.

We report here on the synthesis, crystal structure, and electronic and thermal transport properties of the synthetic $Cu_{26}Ti_2Sb_6S_{32}$ colusite and its Ge substituted derivatives. We successfully placed Ti^{4+} on the T site and substituted Sb^{5+} instead of M cation (Ge^{4+} or Sn^{4+}) (Figure 1a). With this study, we can confirm that the pure compound is semiconducting and that the Ge-substituted series $Cu_{26}Ti_2Sb_{6-x}Ge_xS_{32}$ (x = 1, 2, and 3) exhibit excellent thermoelectric properties with a high ZT value of 0.9 at 673 K, thanks to large $S^2\rho^{-1}$ and low κ_{lat}. Using results from first principles density functional theory calculations of the electronic and phonon dispersions, we rationalize the microscopic mechanisms at the origin of the thermoelectric performance as well as potential applications of this new semiconducting material.

Experimental Section

Sample synthesis. Samples of $Cu_{26}Ti_2Sb_{6-x}Ge_xS_{32}$ (x = 0, 1, 2, and 3) were synthesized by melting the constituent elements. The elements, weighed according to the target compositions, were sealed in an evacuated quartz tube. The tube was heated to 1373 K, maintained at this temperature for 24 h, and subsequently cooled to room temperature. For x = 1–3, the product was manually crushed and then molded into a pellet. The pellet was sealed in an evacuated quartz tube and subjected to heat-treatment at 823 K. Each sample, x = 0 (as melted) and x = 1–3 (heat-treated), was then manually crashed and pulverized by using planetary ball mill (Pulverisette 7 premium line, Fritsch) at a disk rotation speed of 450 rpm for 1 h. The powder was ball-milled in a jar together with seven balls of 10 mm diameter in an Ar atmosphere. The jar and balls were made of tungsten carbide (WC). The obtained powder was loaded into a WC die with an inner diameter of 10 mm, which was placed in a hot-press sintering furnace (PLASMAN CSP-I-03121, S. S. Alloy). The sintering was performed at 773 K over 1 h in a flowing N_2 atmosphere under a uniaxial pressure of 200 MPa. The sintered sample was cut and polished into bars and disks for the measurement of thermoelectric properties.

Sample characterization. Purity and crystal structure, surface morphology, and chemical compositions of sintered $Cu_{26}Ti_2Sb_{6-x}Ge_xS_{32}$ samples were investigated by powder X-ray diffraction (PXRD), high-angle annular dark-field scanning transmission electron microscopy (HAADF-STEM), scanning electron microscopy (SEM), energy dispersive spectroscopy (EDS), and thermogravimetry/differential thermal analyses (TG/DTA).

PXRD data were collected in the range $10° \leq 2\theta \leq 100°$ using a diffractometer (MiniFlex600, RIGAKU) with a Cu K_α radiation source. PXRD data analyses were performed by Rietveld refinement using the FullProf and WinPlotr software packages.[17, 18] Zero-point shift, lattice parameter, peak shape parameters, asymmetry parameters, fractional atomic coordinates, and isotropic displacement parameters were refined after removing background contribution manually. Atomic-resolution observations were performed on powdered samples using a transmission electron microscope (Titan Cubed 60–300 G2, Thermo Fisher Scientific) which is equipped with a spherical aberration corrector (DCOR, CEOS) for the probe-forming lens system. The microscope was operated in the STEM mode at an accelerating voltage of 300 kV. The convergence semi-angle of the electron probe was set to 18 mrad. The typical probe diameter was less than 0.1 nm. An ADF detector was positioned to detect scattered electrons with an angular range from 38 to 184 mrad. SEM and EDS were performed using a microscope (JCM-6000Plus NeoScope, JEOL). TG/DTA were performed on powdered samples in an flowing Ar atomosphere at 300 K–973 K using an analyzer using an analyzer (STA 2500 Regulus, NETZSCH).

Electrical and thermal properties measurements. Electrical resistivity, ρ, and Seebeck coefficient, S, were simultaneously measured by a four-probe DC method and a temperature differential method, respectively, at 300 K–673 K under a low-pressure He atmosphere using a measurement system (ZEM-3, ADVANCE RIKO). Thermal diffusivity α and specific heat C_P were measured by a laser-flash method at 300 K–673 K in a flowing Ar atmosphere using a thermal analyzer (LFA-457 MicroFlash, Netzsch). The absolute values of C_P were derived from a comparison with values measured for a standard sample of Pyroceram 9606 (Netzsch). The C_p values are in agreement or slightly higher than the Dulong–Petit values. These data were used to calculate the thermal conductivity using the relation $\kappa = \alpha C_P d_s$, where d_s is the sample density that has been estimated from dimensions and weight. The Hall-effect measurements were performed using a four-probe DC method in a vacuum chamber (Mottainai energy), with a permanent magnet generating a magnetic field of 0.62 T at 300 K. We calculated n as $R_H^{-1}e^{-1}$, based on the single-carrier model, where R_H is the Hall coefficient and e is the elementary charge.

First principles calculations. Band structure, density of states, and phonon dispersions were computed using the Quantum EXPRESSO package[19] as integrated in AFLOWπ[20] with ultrasoft PBEsol pseudopotentials[21] corrected with a Hubbard U computed within the ACBNo approach as well as the SCAN[22] exchange and correlation functionals (Table S1). The energy band gap is very sensitive to the computational parameters and SCAN provides the best comparison to the experimental data. We chose an energy cut-off of 60 Ry, a 4 × 4 × 4 (shifted) integration grid, and cold smearing. Electronic transport coefficients were evaluated with PAOFLOW.[23] Phonons were computed with the finite difference method using a 2 × 2 × 2 supercell.

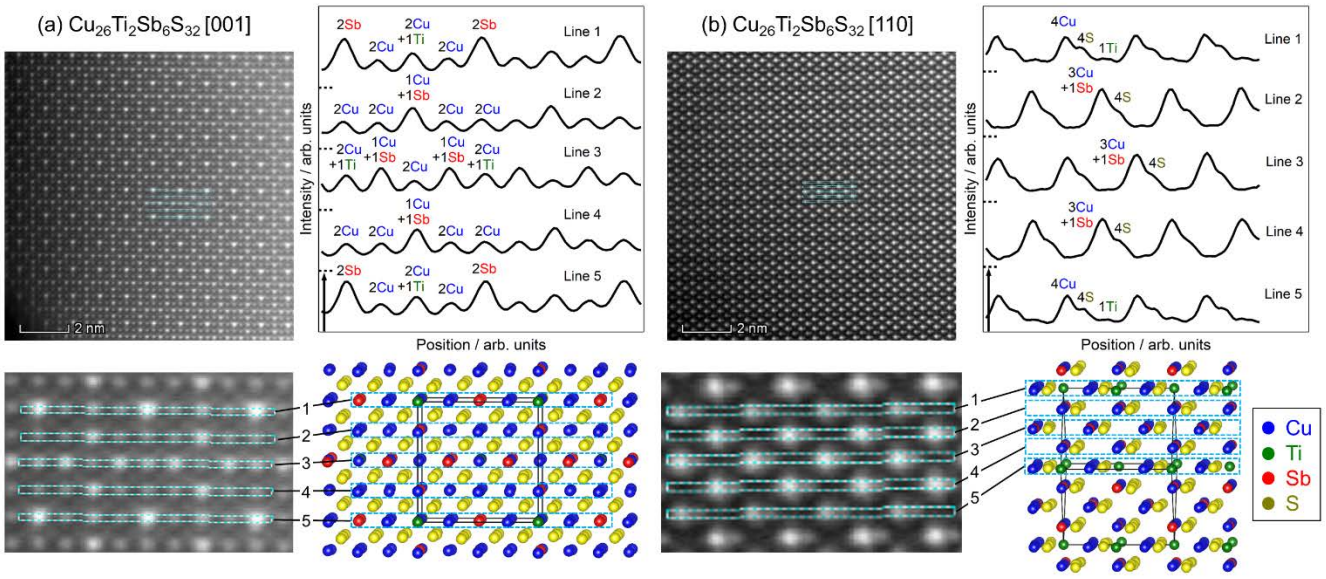

Figure 2. High-angle annular dark-field scanning transmission electron microscopy images of $Cu_{26}Ti_2Sb_6S_{32}$ along (a) [001] and (b) [110] directions. The expanded views of the image and the corresponding views of the colusite structure are shown. Profiles of intensity of atomic columns (spots) for lines denoted by 1–5 are also shown. The label of atomic columns (e.g., 2Cu+Ti) denotes the number of atoms periodically contained in the columns.

Results and Discussion

PXRD patterns of the sintered samples are displayed in Figure 1b. Relative intensities of diffraction peaks for the x = 0 ($Cu_{26}Ti_2Sb_6S_{32}$) sample agree with those of the simulated pattern based on the colusite structure ($P\bar{4}3n$),[24,25] considering the occupation of 6*d*, 8*e*, and 12*f* sites by Cu, 2*a* site by Ti, 6*c* site by Sb, and 8*e* and 24*i* sites by S. The validity of this ordered cationic distribution in the colusite structure is confirmed by (i) the significant intensity of the $h\ k\ l$ reflections with $h + k + l = 2n + 1$ (*e.g.*, 210, 320) indicating important chemical difference (contribution of atomic number Z to X-ray diffracion intensity $I \propto Z^2$) between atoms located on crystallographic sites related one to the other by a [½, ½, ½] translation (i.e. the 6*c* and 6*d* sites occupied by Sb and Cu, respectively), equivalent to that observed in $Cu_{26}V_2Sn_6S_{32}$ colusite (6*c* and 6*d* sites occupied by Sn and Cu, respectively)[13] and (ii) low reliability factors (R_{Bragg} = 4.27, R_F = 9.29, R_{wp} = 4.67, R_{exp} = 5.97) of PXRD Rietveld refinement. Indeed, all attempts to refine the cationic site occupancy between these different sites failed to improve the reliability factors. Thus, bearing in mind that the atomic numbers of the three cations are significantly different, the initial ordered cationic distribution remains the most likely (Figure S1a, Table S2). The ordered distribution of atoms in the colusite structure was also confirmed by HAADF-STEM. The HAADF-STEM images along [001] and [110] directions show well aligned atomic columns (spots) whose positions reasonably agree with those expected from the colusite structure (Figure 2). The intensity of each spot is positively correlated with the square of atomic number (Z^2) of the constituent elements. For the $Cu_{26}Ti_2Sb_6S_{32}$ structure, four types of cation columns are running along the [001] direction labelled 2Sb, 1Cu+1Sb, 2Cu+1Ti, and 2Cu (the label denotes the number of atoms periodically arranged in the columns). The spot's intensity should decrease, from 2Sb to 2Cu in the order mentioned above. The line profile in Figure 2a, indeed, follows this order. Note that the HAADF-STEM image exhibits no mixing of cations (Cu and Sb); such a mixing was observed in the $Cu_{26}T_2Sn_6S_{32}$ (T = V, Nb) colusites.[13,26] Along the [110] direction, there are four types of columns labelled 3Cu+1Sb, 4Cu, 4S, and 1Ti; the HAADF-STEM image and the line profile of intensity (Figure 2b) are in agreement. The 1Ti columns appear as small humps in the line profile of intensity at the expected position for the $Cu_{26}Ti_2Sb_6S_{32}$ structure. The combination of evidences from PXRD and STEM, clearly demonstrates the perfectly ordered $Cu_{26}Ti_2Sb_6S_{32}$ structure.

The sphalerite-like framework is extremely important for the properties of colusites. In $Cu_{26}Ti_2Sb_6S_{32}$, the Cu–S distances are coherent with those reported for $Cu_{26}V_2Sn_6S_{32}$ and $Cu_{26}T_2Ge_6S_{32}$ (T = V, Cr, Mo, W) colusites (Table S2).[11,13] This fact suggests a limited modification/distortion of the CuS_4 tetrahedra in the sphalerite-like framework by the introduction of Ti on the "interstitial" 2*a* position and Sb on the 6*c* site. This effect also supports the conjecture that Sb^{5+} is present in these colusites instead of Sb^{3+}; indeed, the lower formal oxidation state would favor triangular or strongly distorted tetrahedral coordination due to the lone pair of electrons.[27,28] The Sb-S distances of 2.451 Å (see Table S2) are in good agreement with those observed in Cu_3SbS_4 (2.405 Å) which also contains Sb^{5+} exclusively.[16] Finally, the absence of secondary phase in the x = 0 sample confirms the formal charge configuration $Cu^{+}_{26}Ti^{4+}_2Sb^{5+}_6S^{2-}_{32}$ of our initial design. It should be noted that the Ti–Cu distances in the $[TiS_4]Cu_6$ complex are comparable with the T–Cu distances for $Cu_{26}T_2Ge_6S_{32}$ (T = Mo, W),[11] but larger than the Cr–Cu distance for $Cu_{26}Cr_2Ge_6S_{32}$.[11]

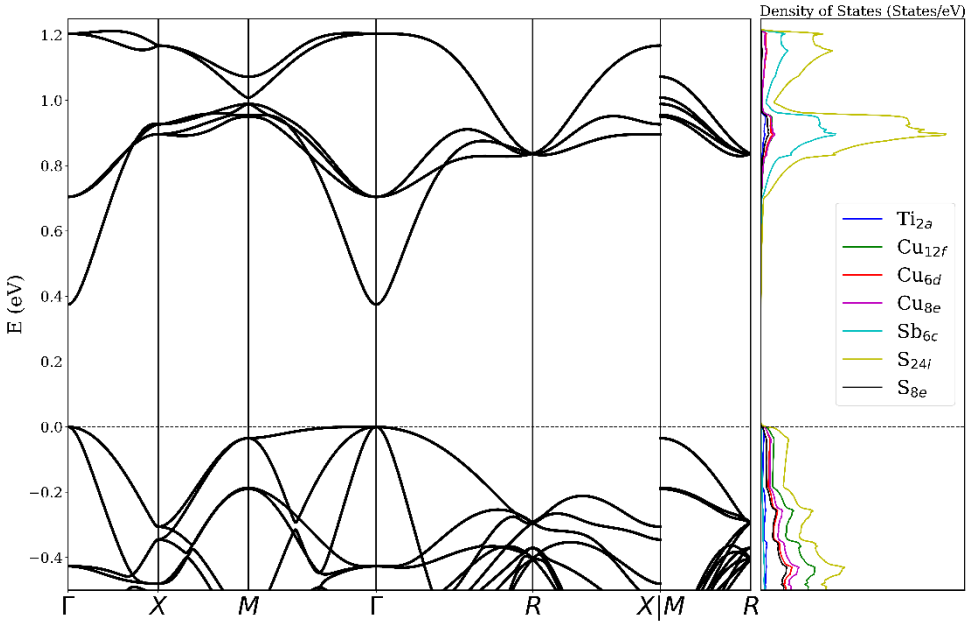

Figure 3. Electronic band dispersion and density of states for $Cu_{26}Ti_2Sb_6S_{32}$.

As for x = 0, the PXRD patterns showed that the x = 1–3 samples are of high purity (Figure S1b-d). Only a small peak attributed to the secondary phase $Cu_{2-\delta}S$ is observed in the x = 2 sample. As Ge content x increases, the peak positions of the colusite phase are shifted to higher angles. This result reflects a decrease in the lattice parameter from 10.7814(2) Å (x = 0) to 10.7014(3) Å (x = 3). The decrease of the intensity of the h k l reflections with $h + k + l = 2n + 1$ (*e.g.*, 210, 320) shows a decrease of the aforementioned chemical difference between the 6*c* site for Sb (Z = 51) and the 6*d* site for Cu (Z = 29). This result proves that Sb is substituted by the lighter element, Ge (Z = 32). Hence, the lattice contraction can be attributed to the smaller ionic radius of Ge^{4+} (0.390 Å) compared to Sb^{5+} (0.565 Å).[29,30] We further confirmed by EDS that the actual chemical distribution of Cu, Ti, Sb, and Ge agrees with the nominal compositions (Table S3). EDS element mapping confirms the homogeneous distribution of Ge (dopant) in the material (Figure S2).

Thermoelectric transport properties were measured for the four samples in the series $Cu_{26}Ti_2Sb_{6-x}Ge_xS_{32}$, whose highly-dense character was confirmed by the relative density values (99–100%) and SEM images (Figure S3). The x = 0 sample exhibits large ρ (1.8×10^6 μΩ m) and S (870 μV K^{-1}) at 300 K (Figure S4) which decrease with T, representative of a semiconducting behavior. For semiconductors, the slope of $\rho(T)$ is an important measure to investigate the activation energy of electron (E_A). Herein, we calculated E_A using the relation $\ln\rho = \ln\rho_0 + E_A/k_BT$, where ρ_0 is the constant and k_B is the Boltzmann constant. A linear fitting of $\ln\rho$ with respect to $1/T$ at temperatures between 350 K and 600 K gave E_A = 0.25 eV. It should be noted that E_A value depends on samples and varies between 0.25 and 0.35 eV. The semiconducting behavior with x = 0 is in agreement with charge compensation ($Cu^{+}_{26}Ti^{4+}_{2}Sb^{5+}_{6}S^{2-}_{32}$), the experimental low hole carrier concentration (n) of 1.7×10^{17} cm^{-3} at room temperature, and theoretical results. A direct energy gap of 0.375 eV at Γ point was determined from the band structure (Figure 3). The order of gap energy is comparable with that of the aforementioned E_A, indicating that the x = 0 sample is in the intrinsic region above 350 K. The electronic density of states (DOS) shows that the top of the valence band (VB) at Γ point is primarily composed of electronic orbitals of Cu and S (Figure 3). Therefore, the electronic transport properties shown below are governed by the tetrahedral Cu–S framework. It is interesting to note the non-degenerate band at the bottom of the conduction manifold: derived from sulfur 4s states, this dispersive band carries very low contribution to the DOS.

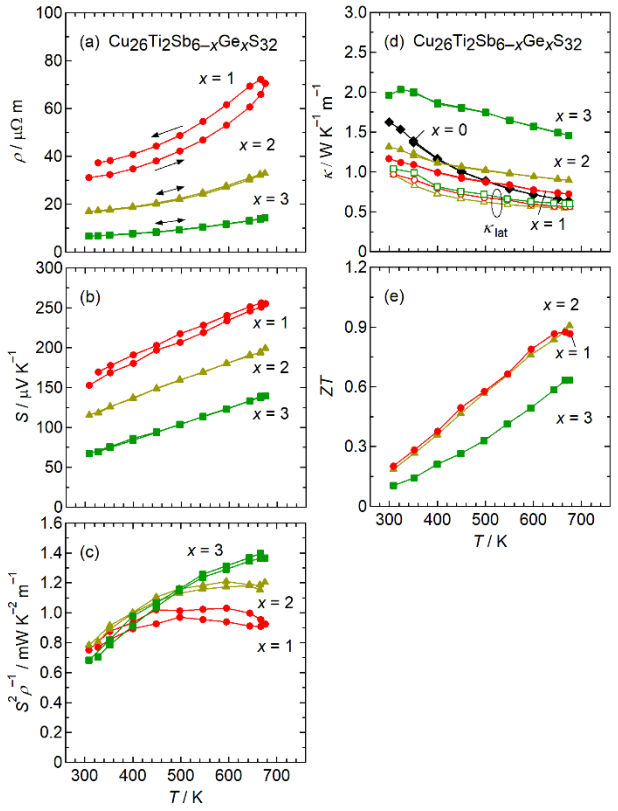

Figure 4. (a) Electrical resistivity ρ, (b) Seebeck coefficient S, (c) power factor $S^2\rho^{-1}$, (d) thermal conductivity κ and its lattice component κ_{lat}, and (e) dimensionless figure of merit ZT for $Cu_{26}Ti_2Sb_{6-x}Ge_xS_{32}$ (x = 1–3). In (d), $\kappa \simeq \kappa_{lat}$ for x = 0 is also shown.

With the substitution of Ge for Sb, holes are introduced in the conductive Cu–S network and the value of ρ at 300 K is suppressed by five orders of magnitude for x = 1 (Figure S4a, Figure 4a) and decreases to 6.6 μΩm for x = 3. Simultaneously, S decreases from 870 μV K^{-1} for x = 0 (Figure S4b) to 150 μV K^{-1} for x = 1 and further decreases to 67 μV K^{-1} at x = 3 at 300 K (Figure 4b). These variations, due to the Ge^{4+} for Sb^{5+} substitution, are consistent with the increase in n with x (n = 1.7 × 10^{17} cm^{-3} for x = 0; 0.8 × 10^{21} cm^{-3} for x = 1; 1.5 × 10^{21} cm^{-3} for x = 2; 3.0 × 10^{21} cm^{-3} for x = 3). In Figure S5, we show the variation of the DOS in the proximity of the energy gap. We modeled explicit Ge doping with few selected supercells. Within our approximations, the effect of Sb substitution on the VB corresponds to an almost rigid shift of the Fermi level as noticeable in Figure S5 and in the transport coefficients (Figure S6).

For x = 1–3, both ρ and S rise upon heating to 673 K, characteristic of degenerate semiconductors. Although the value of n is constant or slightly increases with T, the Hall mobility ($\mu_H = R_H\rho^{-1}$) decreases, leading to the rise of ρ (Figure S7). The μ_H shows $\propto T^{-3/2}$ behavior, indicating that the acoustic phonon scattering is the dominant mechanism of the electron scattering (Figure S7). As a result of these temperature dependences, $S^2\rho^{-1}$ increases from 0.7–0.8 mW K^{-2} m^{-1} at 300 K to 0.9–1.4 mW K^{-2} m^{-1} at 673 K (Figure 4c). Such high $S^2\rho^{-1}$ values obtained for x = 2 and x = 3 are due to the optimum n for these compositions and originate from the specific electronic band dispersion of the VB. Indeed, for the p-type conduction, heavier electron pockets from the M and the Γ points contribute to the transport, resulting in large S as well as high $S^2\rho^{-1}$ as reported for other $Cu_{26}T_2M_6S_{32}$ colusites.[11]

It should be noted that the measurements of ρ and S for x = 0 upon heating (to 673 K) and cooling were not reversible (Figure S4) and color of the sample surface was changed thorough the measurement, indicating partial decomposition of the colusite phase (in a low-pressure He atmosphere in the measurement apparatus). A XRD measurement confirmed the existence of $Cu_{12}Sb_4S_{13}$ and unknown phases, which appared near the surface of the sample (Figure S8). The (partial) decomposition may be induced by the sublimation of sulfur. A small hysteresis was observed in $\rho(T)$ and $S(T)$ also for x = 1 while not for x = 2 and 3, indicating that the Ge substitution improve the thermal stability (Figures 4a, 4b). Indeed, XRD measurements showed no sign of decomposition for x = 2 and x = 3 (Figure S9). One can expect that the decomposition of the pristine sample is promoted by the sublimation of sulfur. However, thermogravimetry/differential thermal analysis for x = 0 and x = 2 in an Ar-flowing atmosphere did not show clear evidence of the sulfur sublimation and decomposition upon heating to 673 K. (Figure S10). Further investigation by *in-situ* PXRD and/or neutron diffraction measurements[31] in various atmosphere is required to establish the phase stability and decomposition mechanisms.

Figure 4d shows the temperature dependence of κ in the series $Cu_{26}Ti_2Sb_{6-x}Ge_xS_{32}$. The value of κ for x = 0, which is dominated by its lattice component κ_{lat}, is 1.6 W K^{-1} m^{-1} at 300 K and decreases to 0.6 W K^{-1} m^{-1} upon heating to 673 K. With the substitution of Ge for Sb, κ decreases for x = 1 at 300 K, and then increases for x = 2 and 3. This trend can be rationalized considering the competition between scattering effects associated with chemical disorder and an increase in the electronic component, κ_{el}. We estimated κ_{el} using the Wiedemann–Franz law, $LT\rho^{-1}$ with L = 1.5 +exp(−|S|/116),[32] for x = 1–3. The equation regarding L is based on the acoustic phonon scattering of electrons, which is consistent with the behaviors in $\rho(T)$ and $\mu_H(T)$ (Figure 4a, Figure S7). As shown in Figure 4d, κ_{lat} for x = 1–3 is 1.0 W K^{-1} m^{-1} at 300 K and decreases to 0.6 W K^{-1} m^{-1} at 673 K. The former value is much lower than those for x = 0 indicating the relevant contribution of the disorder on the Sb/Ge sites.

The intrinsic low κ_{lat} of $Cu_{26}Ti_2Sb_6S_{32}$ is common to many members of the colusite family. The phonon dispersions and atom-resolved vibrational DOS are shown in Figure 5 and point to the presence of optical mode in the frequency range between 50 cm^{-1} and 100 cm^{-1}. Above that frequency range, flat optical modes exist at 110–130 cm^{-1} and 140–160 cm^{-1}. These optical modes lying below 160 cm^{-1} mainly involve the vibrations of Cu, Sb, and S. Although phonon dispersions do not provide direct information on the thermal transport, the existence of a large number of low-lying op-

tical modes may introduce scattering channels that reduces κ_{lat}.[11,33] Using the quasi-harmonic approximation, we computed the mode-resolved Grüneisen parameters, γ. The results indicate large anharmonicity in the low frequency region for the modes involving Cu, Sb, and S (Figure S11). The average γ computed using the three acoustic modes velocities is 1.752 for $Cu_{26}Ti_2Sb_6S_{32}$, which is comparable to γ for the $Cu_{26}T_2M_6S_{32}$ colusites (T = Cr, Mo, W and M = Ge)[11] and $NaSbSe_2$,[28] $NaSbTe_2$,[28] and Mg_3Sb_2[34] with low κ_{lat}. The phonon dispersions and anharmonic nature of the atomic vibration, as well as the aforementioned structural complexity, justify the low κ_{lat} of $Cu_{26}Ti_2Sb_6S_{32}$.

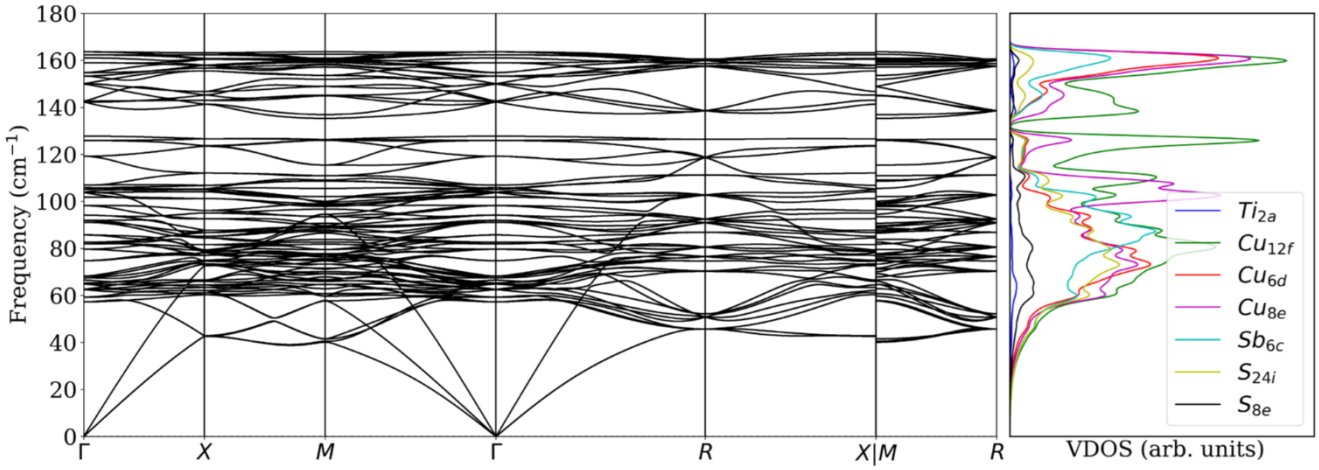

Figure 5. Phonon dispersions and vibrational density of states (VDOS) for $Cu_{26}Ti_2Sb_6S_{32}$.

The potential for application of the new semiconducting compound with the colusite structure is related to the ability to control the p-type doping with the replacement of Sb with Ge. Such a substitution enhances, for instance, the power factor, $S^2\rho^{-1}$, and, because of the low κ (κ_{lat}) leads to figure of merit, ZT up to 0.9 for x = 1 and 2 and 0.6 for x = 3 at 673 K (Figure 4e). This is very remarkable since no specific optimization of the thermoelectric properties has been attempted. The ZT of 0.9 is among the largest reported for environmentally friendly sulfides.[35]

Conclusions

In summary, we have synthesized a new semiconducting sulfide $Cu_{26}Ti_2Sb_6S_{32}$ with the colusite structure by overcoming the difficulties associated with the introduction of 4+ (d^0) cation on the T site and 5+ (d^{10}) cation on the M site. The new compound has been fully characterized and exhibit low thermal conductivity. The partial substitution of Ge^{4+} for Sb^{5+} leads to outstanding thermoelectric power factor. The large ZT achieved in the Ge-substituted material indicate the importance for the field of thermoelectricity. Exploiting the synergy between experiments and theory, we pinpointed the intrinsic mechanisms leading to large $S^2\rho^{-1}$ and low κ_{lat}. The complex cationic distribution and crystal chemistry of $Cu_{26}T_2M_6S_{32}$ colusites provides a fruitful playground to rationally design novel compositions with semiconducting properties.

ASSOCIATED CONTENT

Supporting Information
The Supporting Information is available free of charge at http://pubs.acs.org.

Hubbard U correction computed with the ACBNo approach, Rietveld refinements results of PXRD patterns, Chemical compositions, Elemental mapping of EDS, SEM images, Electrical resistivity and Seebeck coefficient (experiments, calculations), Electronic density of states, TG/DTA data, Mode-resolved Grüneisen parameters

AUTHOR INFORMATION

Corresponding Authors

*__Koichiro Suekuni__ – Department of Applied Science for Electronics and Materials, Interdisciplinary Graduate School of Engineering Sciences, Kyushu University, Kasuga, Fukuoka 816–8580, Japan; Transdisciplinary Research and Education Center for Green Technologies, Kyushu University, Kasuga, Fukuoka 816-8580, Japan; orcid.org/0000-0002-0515-4864; suekuni.koichiro.063@m.kyushu-u.ac.jp

*__Emmanuel Guilmeau__ – CRISMAT, CNRS, Normandie Université, ENSICAEN, UNICAEN, 14000 Caen, France; orcid.org/0000-0001-7439-088X; emmanuel.guilmeau@ensicaen.fr

Authors

__Takashi Hagiwara__ – Department of Applied Science for Electronics and Materials, Interdisciplinary Graduate School of Engineering Sciences, Kyushu University, Kasuga, Fukuoka 816–8580, Japan

__Pierric Lemoine__ – Université de Rennes 1, CNRS, ISCR-UMR 6226, F-35000 Rennes, France; orcid.org/0000-0002-3465-7815

__Andrew R. Supka__ – Department of Physics and Science of Advanced Materials Program, Central Michigan University, Mt. Pleasant, Michigan 48859, USA; orcid.org/0000-0002-9043-1597

Raju Chetty – Global Zero Emission Research Center, National Institute of Advanced Industrial Science and Technology (AIST), Tsukuba, Ibaraki 305-8568, Japan; orcid.org/0000-0003-1072-8241
Bernard Raveau – CRISMAT, CNRS, Normandie Université, ENSICAEN, UNICAEN, 14000 Caen, France
Marco Fornari – Department of Physics and Science of Advanced Materials Program, Central Michigan University, Mt. Pleasant, Michigan 48859, USA; orcid.org/0000-0001-6527-8511
Michihiro Ohta – Global Zero Emission Research Center, National Institute of Advanced Industrial Science and Technology (AIST), Tsukuba, Ibaraki 305-8568, Japan; orcid.org/0000-0002-9093-7117
Rabih Al Rahal Al Orabi – Department of Physics and Science of Advanced Materials Program, Central Michigan University, Mt. Pleasant, Michigan 48859, USA; orcid.org/0000-0001-5880-5838
Katsuaki Hashikuni – Department of Applied Science for Electronics and Materials, Interdisciplinary Graduate School of Engineering Sciences, Kyushu University, Kasuga, Fukuoka 816–8580, Japan; orcid.org/0000-0002-3536-8206
Michitaka Ohtaki – Department of Applied Science for Electronics and Materials, Interdisciplinary Graduate School of Engineering Sciences, Kyushu University, Kasuga, Fukuoka 816–8580, Japan; Transdisciplinary Research and Education Center for Green Technologies, Kyushu University, Kasuga, Fukuoka 816-8580, Japan; orcid.org/0000-0002-1387-5979

Author Contributions

The manuscript was written through the contributions of all authors. All authors have given approval to the final version of the manuscript.

Notes

The authors declare no competing financial interest.

ACKNOWLEDGMENT

This work was financially supported by JSPS KAKENHI Grant No. JP20H02440 (K. S.), and grants from the International Joint Research Program for Innovative Energy Technology funded by METI and Research and Development Program for Promoting Innovative Clean Energy Technologies Through International Collaboration funded by NEDO. E.G. and P.L. acknowledge the financial support of CNRS through the International Emerging Actions program (EXPRESS project).

REFERENCES

(1) Rockett, A.; Birkmire, R. W. $CuInSe_2$ for photovoltaic applications. *J. Appl. Phys.* **1991**, *70*, R81.

(2) Stanbery, B. J. Copper Indium Selenides and Related Materials for Photovoltaic Devices. *Crit. Rev. Solid State Mater. Sci.* **2002**, *27*, 73–117.

(3) Scragg, J. J.; Dale, P. J.; Peter, L. M.; Zoppi, G.; Forbes, I. New routes to sustainable photovoltaics: evaluation of Cu_2ZnSnS_4 as an alternative absorber material. *Phys. Status Solidi B* **2008**, *245*, 1772–1778.

(4) van Embden, J.; Latham, K.; Duffy, N. W.; Tachibana, Y. Near-Infrared Absorbing $Cu_{12}Sb_4S_{13}$ and Cu_3SbS_4 Nanocrystals: Synthesis, Characterization, and Photoelectrochemistry. *J. Am. Chem. Soc.* **2013**, *135*, 11562–11571.

(5) Suekuni, K.; Takabatake, T. Research Update: Cu–S based synthetic minerals as efficient thermoelectric materials at medium temperatures. *APL Mater.* **2016**, *4*, 104503.

(6) Qiu, P.; Shi, X.; Chen, L. Cu-based thermoelectric materials. *Energy Storage Mater.* **2016**, *3*, 85–97.

(7) Powell, A. V. Recent developments in Earth-abundant copper-sulfide thermoelectric materials. *J. Appl. Phys.* **2019**, *126*, 100901.

(8) Suekuni, K.; Kim, F. S.; Takabatake, T. Tunable electronic properties and low thermal conductivity in synthetic colusites $Cu_{26-x}Zn_xV_2M_6S_{32}$ ($x \leq 4$, M = Ge, Sn). *J. Appl. Phys.* **2014**, *116*, 063706.

(9) Suekuni, K.; Kim, F. S.; Nishiate, H.; Ohta, M.; Tanaka, H. I.; Takabatake T. High-performance thermoelectric minerals: Colusites $Cu_{26}V_2M_6S_{32}$ (M = Ge, Sn). *Appl. Phys. Lett.* **2014**, *105*, 132107.

(10) Kikuchi, Y.; Bouyrie, Y.; Ohta, M.; Suekuni, K.; Aihara, M.; Takabatake, T. Vanadium-free colusites $Cu_{26}A_2Sn_6S_{32}$ (A = Nb, Ta) for environmentally friendly thermoelectrics. *J. Mater. Chem. A* **2016**, *4*, 15207–15214.

(11) Pavan Kumar, V.; Supka, A. R.; Lemoine, P.; Lebedev, O. I.; Raveau, B.; Suekuni, K.; Nassif, V.; Al Rahal Al Orabi, R.; Fornari, M.; Guilmeau, E. High Power Factors of Thermoelectric Colusites $Cu_{26}T_2Ge_6S_{32}$ (T = Cr, Mo, W): Toward Functionalization of the Conductive "Cu–S" Network. *Adv. Energy Mater.* **2019**, *9*, 1803249.

(12) Pavan Kumar, V.; Guélou, G.; Lemoine, P.; Raveau, B.; Supka, A. R.; Al Rahal Al Orabi, R.; Fornari, M.; Suekuni, K.; Guilmeau, E. Copper-Rich Thermoelectric Sulfides: Size-Mismatch Effect and Chemical Disorder in the $[TS_4]Cu_6$ Complexes of $Cu_{26}T_2Ge_6S_{32}$ (T=Cr, Mo, W) Colusites. *Angew. Chem. Int. Ed.* **2019**, *58*, 15455–15463.

(13) Bourgès, C.; Bouyrie, Y.; Supka, A. R.; Al Rahal Al Orabi, R.; Lemoine, P.; Lebedev, O. I.; Ohta, M.; Suekuni, K.; Nassif, V.; Hardy, V.; Daou, R.; Miyazaki, Y.; Fornari, M.; Guilmeau, E. High-Performance Thermoelectric Bulk Colusite by Process Controlled Structural Disordering. *J. Am. Chem. Soc.* **2018**, *140*, 2186– 2195.

(14) Bouyrie, Y.; Ohta, M.; Suekuni, K.; Kikuchi, Y.; Jood, P.; Yamamoto, A.; Takabatake, T. Enhancement in the thermoelectric performance of colusites $Cu_{26}A_2E_6S_{32}$ (A = Nb, Ta; E = Sn, Ge) using E-site non-stoichiometry. *J. Mater. Chem. C* **2017**, *5*, 4174–4184.

(15) Klepp, K.; Gurtner, D. Synthesis and crystal structure of Cu_4TiS_4: a novel chalcogenide with tetrahedrally coordinated titanium. *J. Alloys Compd.* **1996**, *243*, 19–22.

(16) Parthé, E.; Garin, J. The crystal structure of Cu3PSe4 and other ternary normal tetrahedral structure compounds with composition $1_3 56_4$. *Acta. Cryst.* **1972**, *B28*, 3672–3674.

(17) Rodríguez-Carvajal, J. Recent advances in magnetic structure determination by neutron powder diffraction. *Physica B Condens. Matter* **1993**, *192*, 55–69.

(18) Roisnel, T.; Rodríguez-Carvajal, J. WinPLOTR: A Windows Tool for Powder Diffraction Pattern Analysis. *Mater. Sci. Forum* **2001**, *378–381*, 118–123.

(19) Giannozzi, P.; Baroni, S.; Bonini, N.; Calandra, M.; Car, R.; Cavazzoni, C.; Ceresoli, D.; Chiarotti, G. L; Cococcioni, M.; Dabo, I.; Dal Corso, A.; de Gironcoli, S.; Fabris, S.; Fratesi, G.; Gebauer, R.; Gerstmann, U.; Gougoussis, C.; Kokalj, A.; Lazzeri, M.; Martin-Samos, L.; Marzari, N.; Mauri, F.; Mazzarello, R.; Paolini, S.; Pasquarello, A.; Paulatto, L.; Sbraccia, C.; Scandolo, S.; Sclauzero, G.; Seitsonen, A. P.; Smogunov, A.; Umari, P.; Wentzcovitch, R. M. QUANTUM ESPRESSO: a modular and open-source software project for quantum simulations of materials. *J. Phys.: Condens. Matter*, **2009**, *21*, 395502.

(20) Supka, A. R.; Lyons, T. E.; Liyanage, L.; D'Amico, P.; Al Rahal Al Orabi, R.; Mahatara, S.; Gopal, P.; Toher, C.; Ceresoli, D.; Calzolari, A.; Curtarolo, S.; Nardelli, M. B.; Fornari, M. AFLOWπ: A minimalist approach to high-throughput ab initio calculations including the generation of tight-binding hamiltonians. *Comput. Mater. Sci.* **2017**, *136*, 76–84.

(21) https://dalcorso.github.io/pslibrary/

(22) Sun, J.; Ruzsinszky, A.; Perdew J. P. Strongly Constrained and Appropriately Normed Semilocal Density Functional. *Phys. Rev. Lett.* **2015**, *115*, 036402.

(23) Buongiorno Nardelli, M. B.; Cerasoli, F. T.; Costa, M.; Curtarolo, S.; De Gennaro, R.; Fornari, M.; Liyanage, L.; Supka, A. R.; Wang, H. PAOFLOW: A utility to construct and operate on ab initio Hamiltonians from the projections of electronic wavefunctions on atomic orbital bases, including characterization of topological materials. *Comp. Mat. Sci.* **2018**, *143*, 462–472.

(24) Spry, P. G.; Merlino, S.; Wang, S.; Zhang, X.; Buseck, P. R. New occurrences and refined crystal chemistry of colusite, with comparisons to arsenosulvanite. *Am. Mineral.* **1994**, *79*, 750–762.

(25) Frank-Kamenetskaya, O. V.; Rozhdestvenskaya, I. V.; Yanulova, L. A. New Data on the Crystal Structures of Colusites and Arsenosulvanites. *J. Struct. Chem.* **2002**, *43*, 89–100.

(26) Suekuni, K.; Shimizu, Y.; Nishibori, E.; Kasai, H.; Saito, H.; Yoshimoto, D.; Hashikuni, K.; Bouyrie, Y.; Chetty, R.; Ohta, M.; Guilmeau, E.; Takabatake, T.; Watanabe, K.; Ohtaki, M. Atomic-scale phonon scatterers in thermoelectric colusites with a tetrahedral framework structure. *J. Mater. Chem. A* **2019**, *7*, 228–235.

(27) Skoug E. J.; Morelli, D. T. Role of Lone-Pair Electrons in Producing Minimum Thermal Conductivity in Nitrogen-Group Chalcogenide Compounds. *Phys. Rev. Lett.* **2011**, *107*, 235901.

(28) Nielsen, M. D.; Ozolins, V.; Heremans J. P. Lone pair electrons minimize lattice thermal conductivity. *Energy Environ. Sci.* **2013**, *6*, 570–578.

(29) Shannon, R. D. Revised effective ionic radii and systematic studies of interatomic distances in halides and chalcogenides. *Acta Crystallogr.* **1976**, *A32*, 751–767.

(30) Chen, K.; Paola, C. D.; Du, B.; Zhang, R.; Laricchia, S.; Bonini, N.; Weber, C.; Abrahams, I.; Yan, H.; Reece, M. Enhanced thermoelectric performance of Sn-doped Cu_3SbS_4. *J. Mater. Chem. C* **2018**, *6*, 8546–8552.

(31) Lemoine, P.; Pavan Kumar, V.; Guélou, G.; Nassif, V.; Raveau, B.; Guilmeau, E. Thermal Stability of the Crystal Structure and Electronic Properties of the High Power Factor Thermoelectric Colusite $Cu_{26}Cr_2Ge_6S_{32}$. *Chem. Mater.* **2020**, *32*, 830–840.

(32) Kim, H. S.; Gibbs, Z. M.; Tang, Y.; Wang, H.; Snyder, G. J. Characterization of Lorenz number with Seebeck coefficient measurement. *APL Mater.* **2015**, *3*, 041506.

(33) Lee, C. H.; Hase, I.; Sugawara, H.; Yoshizawa, H.; Sato, H. Low-Lying Optical Phonon Modes in the Filled Skutterudite $CeRu_4Sb_{12}$. *J. Phys. Soc. Jpn.* **2006**, *75*, 123602.

(34) Zhang, J.; Song, L. ; Sist, M.; Tolborg, K.; Iversen, Bo B. Chemical bonding origin of the unexpected isotropic physical properties in thermoelectric Mg_3Sb_2 and related materials. *Nature Commun.* **2018**, *9*, 4716.

(35) Guélou, G.; Lemoine, P.; Raveau, B.; Guilmeau, E. Recent developments in high-performance thermoelectric sulphides: an overview of the promising synthetic colusites. *J. Mater. Chem. C* **2021**, *9*, 773.

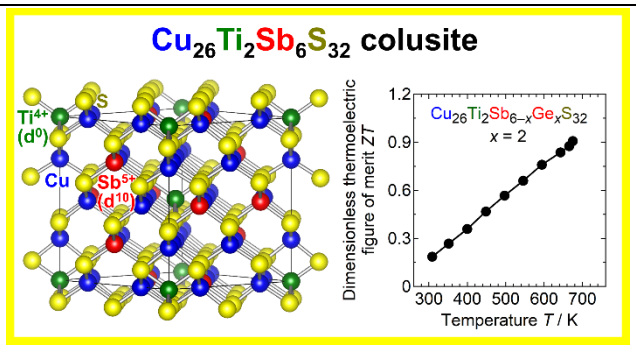

Insert Table of Contents artwork here